NTNU
Norwegian University of
Science and Technology

Prediction of Noise Generated by a Small Helicopter Rotor

Kim Åge Martinussen

Master of Science in Product Design and Manufacturing
Submission date: June 2010
Supervisor: Bernhard Müller, EPT

Norwegian University of Science and Technology
Department of Energy and Process Engineering

Problem Description

Objective:
The objectives of the master project are to understand the physical mechanisms of the generation and propagation of sound of helicopter rotors and to compute the noise generated by a small tail rotor of a helicopter. The numerical results should be validated by comparison with experimental results.

The following questions should be considered in the project work:
1. Understanding of the physical mechanisms of the generation and propagation of helicopter rotor noise.
2. Understanding of the Ffowcs Williams-Hawkings equation and its solutions.
3. Literature review of computational tools for rotor noise prediction.
4. Choice and application of a noise prediction tool to a small tail rotor.
5. Validation of the numerical results by comparison with experimental data.

Assignment given: 01. February 2010
Supervisor: Bernhard Müller, EPT

Preface

This report is the result of my Master's thesis during the spring of 2010. The main topic of the thesis follows from my specialisation project during the autumn of 2009, and was envisioned after a conversation with Trygve F. Marton and Alexander Hall at Prox Dynamics AS, Asker, Norway.

The final scope of the thesis was decided upon by prof. Bernhard Müller and myself. I would like to thank Bernhard Müller for for his invaluable advice and patience. I would also like to thank Trygve F. Marton and Alexander Hall at Prox Dynamics for enabling me to do my Master's thesis on such an exciting topic as aeroacoustics.

Trondheim, June 28th, 2010

Kim Åge Martinussen

Abstract

The fundamental principles of acoustics and of aeroacoustic noise generation are described, along with specific examples relevant for helicopter rotors. The acoustic analogy approach to computing the propagation of sound is presented, and details are given on the Ffowcs Williams-Hawkings (FW-H) equation.

Using an incompressible, laminar Navier-Stokes solver in FLUENT the flow field around a circular cylinder and a NACA 0015 airfoil is computed. The solution of the flows are then used as the input for a simplified FW-H equation.

The simulation results are validated by comparing both the flow parameters and the acoustic solution to numerical data from two different numerical studies. The validation leads to the conclusion that the method used is suitable for the both the flow and noise prediction.

The pressure fluctuations are dominated by convected pressure fluctuations in the flow itself, not that radiated from the source. Due to this the FW-H method was not properly validated by the test cases, and no conclusions can be drawn as to its accuracy.

Sammendrag

Grunnleggende prinsipper for akustikk og aeroakustisk lyd blir beskrevet sammen med eksempler relevante for helikopterrotorer. Akustisk analogi blir presentert som en metode for å beregne propagering av lydbilder, og detaljer gis for Ffowcs Williams-Hawkings- ligningen (FW-H).

Strømningsfeltet rundet en sirkulær sylinder og en NACA 0015 vingeprofil blir beregnet ed hjelp av en inkompressibel laminær Navier-Stokes løser i Fluent. Løsningen benyttes i kilden til en forenklet FW-H ligning.

Resultatene av simuleringene er validert ved å sammenligne både strømningsparametre og den akustiske løsningen med numeriske data fra to forskjellige numeriske studier. Resultatet av validasjonen er at både strømningen og akustikken blir løst med tilfredsstillende nøyaktighet.

Trykkvariasjonene i beregningsdomenet er dominert av strømningsløsningen, og ikke trykkfluktuasjonene som sendes ut fra kilden. Det medfører at FW-H implementasjonen i Fluent ikke ble skikkelig validert, og ingen konklusjoner kan trekkes til dens nøyaktighet.

Contents

1 Introduction **1**
1.1 Micro UAV . . . 1
1.2 Aeroacoustics . . . 2

2 Physical mechanisms of rotor noise **4**
2.1 Basics of acoustics . . . 4
2.2 Physical mechanisms of rotor noise . . . 4
2.2.1 Discrete frequency noise . . . 5
2.2.2 Broadband noise . . . 5
2.2.3 Vibrating sources . . . 6

3 Governing equations **7**
3.1 Fluid mechanics . . . 7
3.1.1 Navier-Stokes equations . . . 7
3.2 Aeroacoustics . . . 8
3.2.1 Direct numerical simulation of acoustics . . . 8
3.2.2 Acoustic analogy . . . 8
3.2.3 Ffowcs Williams-Hawkings equation . . . 9

4 Numerical methods **11**
4.1 Literature review of computational tools . . . 11
4.2 Finite volume method . . . 12
4.2.1 Overview of the finite volume method . . . 12
4.2.2 Approximating values of the discretised variables . . . 13

5 Test cases **14**
5.1 Set up and overview of test-cases . . . 14
5.2 Cylinder . . . 15
5.2.1 Grid . . . 15
5.2.2 Boundary conditions . . . 16
5.3 NACA0015 airfoil . . . 16
5.3.1 Grid . . . 16
5.3.2 Boundary conditions . . . 18

6 Results and discussion **20**
6.1 Cylinder 20
6.1.1 Flow 20
6.1.2 Acoustics 21
6.2 Airfoil 24
6.2.1 Flow 24
6.2.2 Acoustics 26

7 Conclusion **30**

Chapter 1

Introduction

1.1 Micro UAV

A micro UAV is a small unmanned aerial vehicle, with a typical size between 10 cm and 1 m. The size of the UAV is measured as length, wing span or rotor diameter depending on the type of UAV. This master thesis will primarily focus on micro helicopters, although most of the theory is valid for a general aeroacoustic problem.

UAVs and micro UAVs can perform many tasks where using a manned vehicle is not possible or realistic. This could be due to the security risks involved, sizes required or nature of the task.

The MQ-1 Predator, best known for its use in the wars in Afghanistan and Iraq, is an example of using a UAV in a high-risk environment. The Predator is not autonomous, but controlled from operators on the ground. Other well known UAVs include the NASA Pathfinder and Helios projects, designed to perform research from a high altitude and the Insitu Aerosonde designed for atmospheric research at low altitudes.

The Aerosonde is capable of autonomous flight, and it was the first UAV to cross the Atlantic ocean. The flight lasted more than 26 hours, showing another advantage of UAVs. One practical use for this is hurricane monitoring, for example by measuring the conditions in the centre of the hurricane.

Other applications of UAVs include bridge inspection, fire fighting and police operations. A micro UAV can for example enter potentially dangerous areas during a police or military operation. Equipped with regular or infra-red cameras they can then identify potential threats and avoid human casualties.

This last example can, and is, also being used for military purposes, providing soldiers with information. An extension of this is intelligence and espionage, using UAVs to gain access to restricted areas.

Although the popularity of micro UAVs is increasing, there still is much research to be done before their aerodynamic- and aeroacoustic- properties are fully under-

stood. Most of the existing research has been performed on larger vehicles, which places it in an altogether different flow regime as determined by the Reynold's number.

PD-100 Black Hornet The PD-100 is a rotary wing nano helicopter developed by Prox Dynamics, Asker, Norway. It has a single main rotor, complimented by a tail rotor to counteract the torque generated by the main rotor. The helicopter has a mass of about 15 g, a main rotor diameter of 110 mm and a tail rotor diameter of 30 mm. The nominal rate of rotation is 85 Hz for the main rotor and 250 Hz for the tail rotor. The chord lengths are 10 mm and 3 mm respectively. From this we can compute the nominal tip Reynolds number:

$$u_{tip-tail} = O_{tail} \cdot f_{tail} = 2\pi \cdot \frac{0.03\,\mathrm{m} \cdot 250\,\frac{1}{\mathrm{s}}}{2} \approx 23.56\,\frac{\mathrm{m}}{\mathrm{s}}$$

$$\mathrm{Re}_{tip-tail} = \frac{u_{tip-tail} \cdot c_{tail}}{\nu} = \frac{23.56\,\frac{\mathrm{m}}{\mathrm{s}} \cdot 0.003\,\mathrm{m}}{1.46 \cdot 10^{-5}\,\frac{\mathrm{m}^2}{\mathrm{s}}} \approx 5 \cdot 10^3 \tag{1.1}$$

$$\mathrm{Re}_{tip-main} = \frac{85\,\frac{1}{\mathrm{s}} \cdot 2\pi \cdot \frac{0.11\,\mathrm{m}}{2} \cdot 0.1\,\mathrm{m}}{1.46 \cdot 10^{-5}\,\frac{\mathrm{m}^2}{\mathrm{s}}} \approx 2 \cdot 10^5 \tag{1.2}$$

where

$$\begin{aligned} u &= \text{velocity} \\ O &= \text{circumference} \\ f &= \text{frequency (of rotation)} \\ c &= \text{chord length} \\ \nu &= \text{kinematic viscosity } \left(= \tfrac{\rho}{\mu}\right) \\ \mathrm{Re} &= \text{Reynolds number} \end{aligned}$$

The tip Reynolds numbers represent the maximum Reynolds numbers of a rotor blade. Towards the hub the Reynolds number will naturally decrease as the velocity approaches zero. Both the main and the tail rotor will probably see a transition from laminar to turbulent flow, the transition point being dependent on several factors, such as free-stream turbulence, angle of attack, acoustic noise and airfoil geometry [1].

1.2 Aeroacoustics

Aeroacoustics is a multi-physical discipline combining fluid mechanics and acoustics. The name aeroacoustics is derived from aerodynamics and acoustics. The discipline saw its birth in the 1930s, and saw moderate progress during the next decades. In 1952 Lighthill introduced the acoustic analogy-approach [2], allowing jet noise to be estimated.

By expanding on this, Ffowcs Williams and Hawkings arrived at a generalized equation for the propagation of sound from arbitrary moving bodies, as described

in their paper of 1969 [3]. Several areas of aeroacoustics benefited greatly from this, among them the prediction of propeller and rotor noise. More details on the Ffowcs Williams-Hawkings-equation will be presented in section 3.2.3. In this thesis the acoustic analogy approach will be applied to flows relevant to sound-generation from low Reynolds number flows.

Chapter 2

Physical mechanisms of rotor noise

2.1 Basics of acoustics

Definition 1. *Acoustics may be defined as the generation, transmission and reception of energy as vibrational waves in matter.* [4]

The acoustic sources in the wave equation can be split into three separate terms, each representing a different type of source term. These are monopole, dipole and quadrupole terms. A monopole generates sound as if a single point is excited. A dipole consists of two monopoles pulsating at opposite phase of each other, and quadrupole corresponds to two dipoles.

Using this we can classify some sources of noise: Mass injection, corresponding to an enclosed loudspeaker, explosions, and other acoustic sources involving a change in volume, can generate any of the above source terms. In particular a monopole term is often dominating.

Shear forces on surfaces, generated by bodies moving through a fluid, create a dipole source. Guitar strings and free loudspeaker membranes are good examples for this kind of noise source.

Finally free flow shear forces, generated by fluids moving in relation to each other, create quadrupole sources. These originate from the nonlinear term in the Navier-Stokes equations (3.1), and were first described by Lighthill in 1952 [2].

2.2 Physical mechanisms of rotor noise

Helicopter rotor noise is generated by several different phenomena, both vibration noise and various flow induced noise sources. In this chapter an overview of these will be presented, in particular the thickness and loading noise, blade-vortex interaction noise, non-deterministic ingestion noise and vibrational noise.

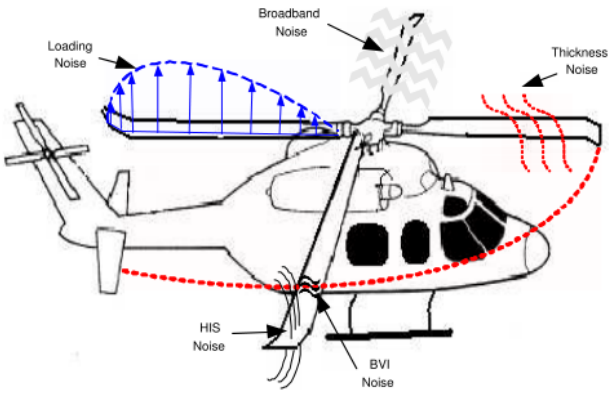

Figure 2.1: Illustration of noise sources on a helicopter rotor [5]

2.2.1 Discrete frequency noise

Discrete frequency noise can be divided into the deterministic components of loading noise and thickness noise, as well as high-speed impulsive noise [6]. The latter is caused by transonic flow around an advancing blade. The PD-100 will have a maximum rotational tip velocity at the main rotor of approximately 60 m/s, plus a maximum forward velocity of around 10 m/s. Thus the total tip velocity is much lower than the speed of sound (≈ 340 m/s), and high-speed impulsive noise can be neglected. This is usually true for most micro UAVs.

Thickness noise is caused by the displacement of air as the blade travels through it. Loading noise on the other hand is caused by the accelerating forces on the air as the blade generates lift. Both of these sources of noise can generally be considered to be harmonic. There are also some non-harmonic loading sources, these are treated separately.

2.2.2 Broadband noise

One non-harmonic loading source is known as blade-vortex interaction (BVI) noise. It is generated by a blade interacting with a vortex shed by the previous blade. For propellers, and also for many modes of rotor flight, these vortices are carried fast enough downstream to avoid this interaction. However while a helicopter is descending, or sometimes even while in hover, the vortices may not be carried far enough downstream to avoid interaction between the rotor blades and the vortices, causing BVI noise to be generated.

Broadband noise is generated when the propeller encounters unstable air, such as atmospheric turbulence or blade wakes. This also gives rise to loading noise terms, but as mentioned above they are considered separate to the harmonic sources.

These non-harmonic noise sources will not be included in the simulations performed in this thesis. All test cases have steady, turbulence free, inlet conditions.

2.2.3 Vibrating sources

Vibrating noise sources are the most common sources of sound. Some common examples are loudspeakers, vocal folds and guitar strings. Any object that vibrates is in fact a sound source, but for humans to hear the emitted sound it must generate sound waves lying within the hearing threshold of 20 Hz to 20 kHz.

There are several sources of vibration on a helicopter, rotating and moving parts, dynamic rotor load, and air interacting with the body itself being major contributors. The rotor blades themselves are flexible, and will be deforming under the dynamic load they are subjected to. This deforming blade is not only a sound source in itself, but also changes the airflow around it, which may cause additional noise generated by the airflow. This coupled interaction of fluid mechanics, elastics and acoustics is beyond the scope of this thesis.

Chapter 3

Governing equations

3.1 Fluid mechanics

3.1.1 Navier-Stokes equations

The Navier-Stokes equations are given by [7]:

$$\rho \frac{Dv_i}{Dt} = F_i - \nabla p + \frac{\partial}{\partial x_j}\left[\mu\left(\frac{\partial v_i}{\partial x_j} + \frac{\partial v_j}{\partial x_i}\right) + \delta_{ij}\lambda\frac{\partial v_i}{\partial x_i}\right] \tag{3.1a}$$

$$\frac{\partial \rho}{\partial t} + \frac{\partial}{\partial x_i}(\rho v_i) = 0 \tag{3.1b}$$

where

$$\begin{aligned}
v &= \text{velocity} \\
t &= \text{time} \\
\rho &\text{density} \\
p &= \text{pressure} \\
x &= \text{spatial coordinates} \\
\mu &= \text{kinematic viscosity} \\
\delta_{ij} &= \begin{cases} 1, & 1 = j \\ 0, & \text{else} \end{cases} \\
\lambda &= \text{second coefficient of viscosity} \\
F_i &= \text{external forces, such as gravity}\,(\rho g_i)
\end{aligned}$$

(3.1a) being the momentum equations and (3.1b) being the continuity equation. The Navier-Stokes equations, along with the energy equation, are believed to fully describe all scales of fluid flow, as long as the fluid can be considered continuous.

For low Mach number flows, incompressible flow can be assumed. This assump-

tion simplifies (3.1b) to

$$\frac{\partial v_i}{\partial x_i} = 0 \tag{3.2}$$

From this we can see that the final term in the momentum equation (3.1a) vanishes. If constant μ is also assumed the momentum equation becomes:

$$\rho \frac{Dv_i}{Dt} = F_i - \nabla p + \frac{\partial}{\partial x_j} \left[\mu \left(\frac{\partial v_i}{\partial x_j} + \frac{\partial v_j}{\partial x_i} \right) \right] \tag{3.3}$$

For a micro UAV incompressible flow and constant μ can usually safely be assumed, although caution should be exercised if combustion processes are involved or the velocities are high.

3.2 Aeroacoustics

3.2.1 Direct numerical simulation of acoustics

Since the Navier-Stokes equations are believed to accurately model the behaviour of fluids, and sound is pressure waves in a fluid, the compressible Navier-Stokes equations will also solve the acoustic field given sufficient spatial and temporal resolution. This is, however, computationally expensive due to the constraints enforced on the size of the grid cells and on the time step.

The regions close to bodies require a fine grid to compute an accurate flow solution. Farther away from any bodies the flow will usually have much smaller gradients, and a coarse grid is sufficient. However, the acoustic solution is still limited by wave length and frequency enforcing a fine grid even in the far-field.

Often flow-solvers use a dissipative upwind scheme to compute the Navier-Stokes equations, since this ensures robustness by aiding the stability of the solution by damping any oscillations or irregularities. With such a solver the acoustic pressure waves will also be subject to dissipation, leading to an incorrect solution.

Boundary conditions are another challenge when using the Navier-Stokes equations to solve the acoustic field, as preventing artificial reflection and other non-physical phenomena from occuring at the boundaries is not trivial.

3.2.2 Acoustic analogy

The acoustic analogy approach, pioneered by Lighthill, provides a link between the flow field and the sound generated by it. The method solves for the acoustic solution separate from the flow field, using the flow field solution as the input of the acoustic equations. It should be noted that any acoustic sources term can be the input in an acoustic analogy equations, not just fluid flow.

There are several advantages to using this method. The most significant being that the acoustic solution no longer depends on the grid, so the grid can be optimised for solving the flow. Another advantage is independence of boundary conditions on the edge of the domain, eliminating artificial reflection and sound generation there.

Among the disadvantages to using the acoustic analogy approach are requiring a free line of sight between the source and the receiver and a lack of accuracy compared to more direct methods. Compared to empirical models the acoustic analogy approach is still computationally expensive as it requires an accurate unsteady flow solution.

Lighthill equation Below follows a short derivation of the Lighthill equation [8]. Lighthill's equation is derived from the Navier-Stokes equations (3.1). By neglecting gravity (3.1a) can be written as:

$$\frac{\partial}{\partial t}\left(\rho v_i\right) + \frac{\partial}{\partial x_j}\left(p_{ij} + \rho v_i v_j\right) = 0 \tag{3.4}$$

where $p_{ij} = p'\delta_{ij} - \tau_{ij}$, with p' being the fluctuating pressure and τ_{ij} being the total stress tensor $\sigma_{ij} - p\delta_{ij}$. σ_{ij} is the residual stress tensor.

By subtracting $\partial/\partial x_i$ applied to (3.4) from $\partial/\partial t$ applied to (3.1b), and reordering the equation we get:

$$\frac{\partial^2 \rho}{\partial t^2} = \frac{\partial^2}{\partial x_i \partial x_j}\left(p_{ij} + \rho v_i v_j\right)$$

We then subtract $c^2\nabla^2\rho$ from both sides and introduce Lighthill's stress tensor $T_{ij} = \rho v_i v_j + p_{ij} - c^2\rho'\delta_{ij}$, to get the Lighthill equation.

$$\frac{\partial^2 \rho'}{\partial t^2} - c^2\nabla^2\rho' = \frac{\partial^2 T_{ij}}{\partial x_i \partial x_j} \tag{3.5}$$

which has the following solution, where $\boldsymbol{y}$ is the position vector of the sound emitter and $\boldsymbol{x}$ is the position vector of the receiver:

$$\rho'\left(\boldsymbol{x}, t\right) = \frac{\partial^2}{\partial x_i \partial x_j}\int_V \frac{T_{ij}\left(\boldsymbol{y}, t - \frac{|\boldsymbol{x}-\boldsymbol{y}|}{c}\right)}{4\pi c^2\left|\boldsymbol{x}-\boldsymbol{y}\right|} d^3\boldsymbol{y} \tag{3.6}$$

3.2.3 Ffowcs Williams-Hawkings equation

Ffowcs Williams and Hawkings generalised Lighthills equation to be valid for sound emission from a general moving surface. This surface can be arbitrarily defined, and all sources within the sources will be accounted for. Sources outside the surface are not included in the FW-H equation, except for a quadrupole term.

The FW-H equation is given as [8]

$$\begin{aligned}\frac{\partial^2}{\partial t^2}\left(H\rho'\right) - c^2\nabla^2\left(H\rho'\right) =& \frac{\partial^2\left(HT_{ij}\right)}{\partial x_i \partial x_j} \\ &- \frac{\partial}{\partial x_i}\left(\left(\rho v_i\left(v_j - u_j\right) + p_{ij}\right)\frac{\partial f}{\partial x_j}\delta\left(f\right)\right) \\ &+ \frac{\partial}{\partial t}\left(\left(\rho\left(v_i - u_i\right) + \rho_0 u_i\right)\frac{\partial f}{\partial x_i}\delta\left(f\right)\right)\end{aligned} \tag{3.7}$$

where

$$H = \begin{cases} 0 & , f < 0 \\ 1 & , f \geq 0 \end{cases} \qquad \text{Heaviside function}$$

$$\delta(f) = \begin{cases} 1, & f = 0 \\ 0, & \text{elsewhere} \end{cases} \qquad \text{Dirac delta function}$$

A general solution to the equation above is

$$\begin{aligned} 4\pi c^2 H \rho'(\boldsymbol{x}, t) = & \frac{\partial^2}{\partial x_i \partial x_j} \int_V \frac{J T_{ij}}{r\,|1 - M_r|} d^3\boldsymbol{\eta} \\ & - \frac{\partial}{\partial x_i} \int_S \frac{\rho v_i (v_j - u_j) + p_{ij}}{r\,|1 - M_r|} n_j K dS(\boldsymbol{\eta}) \\ & + \frac{\partial}{\partial t} \int_S \frac{\rho (v_i - u_i) + \rho_0 u_i}{r\,|1 - M_r|} n_i K dS(\boldsymbol{\eta}) \end{aligned} \tag{3.8}$$

where

$$d^3\boldsymbol{y} = J d^3\boldsymbol{\eta}$$

$$K = J \frac{\left|\text{grad}_y f\right|}{\left|\text{grad}_\eta f\right|}$$

In Fluent the volume integral, representing the quadrupole term, is neglected. The reasoning behind this is that for subsonic flows the quadrupole source term is small. If volume sources are large enough to warrant inclusion this can be achieved by placing $f = 0$ some distance away from the surface of the body itself. This creates an artificial sound emitting surface, and both monopole, dipole and quadrupole sound sources inside this surface will be accounted for.

Chapter 4

Numerical methods

4.1 Literature review of computational tools

To numerically solve the equations presented in Chapter 3 some sort of CFD (computational fluid dynamics) tool is required. CFD tools can be classified in several different ways, for example by their numerical methods, type of user input or intended application area, all of whom are coupled to some degree.

Classified by application area there are two main classes of CFD software, divided by the type of solvers they use: those with general solvers and those with specialised solvers. The general solvers are designed to handle a wide variety of flow-problems and are usually robust. Specialised solvers on the other hand are tailor made for a specific application area. This allows for optimisations in accuracy, robustness and/or speed compared to the general solvers.

Some common general purpose CFD software include CFX and Fluent from Ansys, STAR CCM+ from CD-adapco and OpenFOAM from OpenCFD. An example of a solver specialised for helicopters is GenHel.

It was decided that general purpose CFD software was desired, as this enables extending the simulations to include more effects if needed. No candidates stood out as being the optimal choice, with most of the available software containing both adequate low Reynolds number solvers and a FW-H model. Among the alternatives Fluent was chosen as the author has previous knowledge of using this software. Fluent was used for performing both the flow simulations and the acoustic computations.

Among the post-processors MatLab stood out as a flexible and powerful tool, and will compliment the post-processing available in Fluent.

4.2 Finite volume method

4.2.1 Overview of the finite volume method

The finite volume method is based on dividing the computational domain into small volumes and solving the relevant conservation equations in integral form for each of these volumes. To do this the data at the borders of the small volumes is approximated using values from some or all of the neighbouring volumes.

The transport equation for some scalar ϕ is given as:

$$\int_{\Omega} \frac{\partial \rho \phi}{\partial t} dV + \int_{\partial \Omega} \rho \phi \boldsymbol{v} \cdot d\boldsymbol{A} = \int_{\partial \Omega} \Gamma_{\phi} \nabla \phi \cdot d\vec{A} + \int_{\Omega} S_{\phi} dV \tag{4.1}$$

where

$$\begin{aligned}
\Omega &= \text{domain of a control volume} \\
\partial \omega &= \text{boundary of a control volume} \\
\rho &= \text{density} \\
\boldsymbol{v} &= \text{velocity vector} \\
\boldsymbol{A} &= \text{surface area vector} \\
\Gamma_{\phi} &= \text{diffusion coefficient for } \phi \\
\nabla \phi &= \text{ gradient of } \phi \\
S_{\phi} &= \text{source of } \phi \text{ per unit volume}
\end{aligned}$$

This is then discretised to

$$\frac{\partial \rho \phi}{\partial t} V + \sum_{f}^{N_{faces}} \rho_f \vec{v}_f \phi_f \cdot \vec{A}_f = \sum_{f}^{N_{faces}} \Gamma_{\phi} \nabla \phi_f \cdot \vec{A}_f + S_{\phi} V \tag{4.2}$$

where

$$\begin{aligned}
N_{faces} &= \text{number of faces enclosing cell} \\
\phi_f &= \text{value of } \phi \text{ convected through face } f \\
\rho_f \vec{v}_f \cdot \vec{A}_f &= \text{mass flux through the face} \\
\vec{A}_f &= \text{vectorarea of face } f, \\
\nabla \phi_f &= \text{gradient of } \phi \text{ at face } f \\
V &= \text{cell volume}
\end{aligned}$$

The first term, $\frac{\partial \rho \phi}{\partial t}$, is then discretised using some discretisation scheme in time. The simulations performed in this thesis use a second order implicit scheme, namely the second order backward differentiation formula for $\frac{\partial \rho \phi}{\partial t} = F(\phi)$:

$$\frac{3\phi^{n+1} - 4\phi^{n} + \phi^{n-1}}{2\Delta t} = F\left(\phi^{n+1}\right) \tag{4.3}$$

Here the superscripts indicate which time level the value is taken at. As F is taken at the same time level $(n+1)$ as is currently begin computed this is an implicit scheme. Implicit schemes are unconditionally stable with respect to time step size for linear problems, but for non-linear problems they too are restricted by the time step size. It should also be noted that the numerical error may be dependent on the size of the time step, so ensuring stability is not sufficient [9].

The CFL criterion is useful for determining whether or not the time step is sufficiently small. It describes the relationship between the distance the flow moves in one time step, and the size of the cells.

$$C \leq \sum_i \frac{v_i \Delta t}{\Delta x_i} \rightarrow \Delta t \leq \sum_i \frac{C \Delta x_i}{v_i} \tag{4.4}$$

where the Courant number C is determined by the problem. $C = 1$ corresponds to the flow using one time step to flow through one cell. This has been chosen as the limiting CFL criterion, although larger Courant numbers could usually be accepted.

4.2.2 Approximating values of the discretised variables

The QUICK scheme was used to discretise the spatial terms of the momentum equation. QUICK is an acronym for *quadratic upstream interpolation for convective kinetics.* The QUICK scheme is best suited for structured grids, as it relies on interpolation to determine values at the cell faces. To avoid this problem FLUENT switches to a second order upwind scheme if the grid is unstructured. For a hybrid grid, a grid consisting of a combination of structured and unstructured grid cells, FLUENT will use the appropriate scheme for each part of the grid [10].

The QUICK-scheme was chosen as a high degree of accuracy was desired near the body, and the QUICK-scheme is a third-order scheme. It should be noted that other schemes were not tested.

Since we have four equations (three momentum plus continuity) and four unknown variables (three velocities and pressure) the system is fully determined. However no good link exists between the pressure and the velocity. Therefore a pressure-velocity coupling is needed, in this case the SIMPLEC method.

Now, we can first solve the momentum equations using some guessed pressure, and then use the SIMPLEC method to correct the pressure based on the calculated velocity estimates.

SIMPLEC stands for SIMPLE-Consistent, and is almost identical to the SIMPLE *(semi-implicit method for pressure-linked equations).* The difference between the two algorithms lies in the simplifications in the velocity- and pressure-correction equations. The pressure itself was discretised using a second order scheme.

More details on the finite volume method, QUICK, SIMPLEC and other numerical details can be found in [11].

Chapter 5

Test cases

5.1 Set up and overview of test-cases

To validate the solution obtained using FLUENT different cases were tested. First two-dimensional flow around a circular cylinder at Re = 200 and Re = 150, both at Mach number 0.2, and second a two-dimensional flow around a NACA 0015 airfoil at Re = 300 at Mach number 0.2 and angle of attack α of 20°.

Two-dimensional flow around a cylinder is a well studied case, which means experimental and numerical results are abundant. In addition the simple geometry makes it easier to adjust the grid and observe what effects various grid configurations have on the final solution.

The NACA 0015 airfoil test case presents an asymmetric problem with a more complex flow pattern, and therefore is more directly relevant to rotor noise. It still does not include three dimensional effects or unsteady inlet boundary conditions. In other words it is primarily the thickness and loading noise for which FLUENT will be validated.

The reference values to the Re = 200 cylinder case and the NACA 0015 airfoil case were extracted from an article by Zhen, Michelsen and Sørensen[12], except values for C_d for the Re = 200 cylinder which are given in [13]. The reference values to the Re = 150 cylinder case were found from an article by Müller[14].

Once the grids are generated the time step Δt will be constrained by the CFL-condition (4.4), with a Courant number of $C = 1$. See section 4.2.1

The velocities at the inlets were determined by the Reynolds number

$$\mathrm{Re} = \frac{v_\infty L}{\nu} \tag{5.1}$$

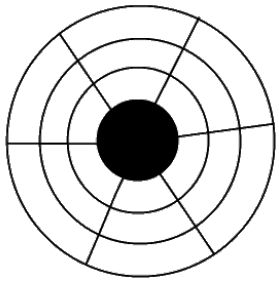

Figure 5.1: Example of a simple O-grid

5.2 Cylinder

5.2.1 Grid

The grid was meshed using a hybrid grid approach, with an O-grid in the region close to the cylinder and an unstructured grid farther out towards the boundary. The reason for not using an O-grid for the entire domain lies in how FLUENT handles boundary conditions.

FLUENT prefers that the boundaries are either pure inlets or pure outlets for incompressible flow. An O-grid would have regions where the inlet is almost parallel to the direction of the flow, as the outer boundary of an O-grid by nature is circular or elliptical. Greater control of the shape of the outer boundaries are obtained by using an unstructured grid outside the O-grid.

The O-grid consists of 200 cells both in the circumferential and radial direction, extending from $r = 0.5$ m, the boundary of the cylinder, to at $r = 10$ m, resulting in a total of 40000 cells for the O-grid. The innermost cells have $\Delta r = 0.0066$ m and $\Delta\theta = 0.0157$ m, growing to $\Delta r = 0.156$ m and $\Delta\theta = 0.314$ m at $r = 10$ m.

The unstructured grid consists of a total of 27000 cells, filling the gap between $r = 10$ m and the outer boundary of the computational domain at $y = \pm 30$ and $(-20 < x < 40)$. The grid is shown in figure 5.2

The cylinder itself is situated in the centre of the O-grid, and has a diameter of $D = 1$ m. The two black circles in the top figure (5.2a) represent the location of the sound receivers, located at $(x, y) = (12, 0), (0, 12)$ and $(0, -12)$.

As described in section 3.2.2, solving the acoustics field using the Ffowcs William-Hawkings equation eliminates the need for a fine grid in the far-field region, and also avoids any boundary effects on the sound. Due to this the grid is optimised for solving the flow around the cylinder, while reducing the total number of cells to speed up the calculation. This can be seen by the grid having small cells near the cylinder, growing larger out towards the boundaries.

An adapted mesh was generated by refining the grid within $x \pm 2.1$m and $y \pm 2.1$m. Using the adaptation tools available in Fluent the cells in the inner region were each

split into four smaller cells, halving $\Delta\theta$ and Δr for each cell in the adapted region. The adapted grid has a total of 145000 cells. The simulation on the adapted mesh was initiated from the solution obtained at the original mesh.

5.2.2 Boundary conditions

The boundary condition at the outlet was chosen as pressure outlet with 0 gauge pressure. The inlet was set up as a velocity inlet, with the velocity magnitude determined by the Reynolds number. $\mathrm{Re} = 150 \rightarrow v_\infty = 0.00255\ \frac{\mathrm{m}}{\mathrm{s}}$ and $\mathrm{Re} = 200 \rightarrow v_\infty = 0.00356\ \frac{\mathrm{m}}{\mathrm{s}}$.

Due to the problem of parallel boundaries mentioned above, the flow was sent in at an angle, $\alpha = 5°$, in relation to the x-axis. This ensures that the bottom and left boundaries are inlets and the top and right boundaries are outlets. No-slip boundary was used for the cylinder itself, meaning that $u_{\mathrm{wall}} = 0$.

Using the CFL condition (4.4) at a cell at the top of the cylinder an estimate for Δt was found. v_x was conservatively estimated to be $2 \cdot V_\infty$, and v_y estimated to be 0.

$$\Delta t = \frac{C\Delta\theta}{2 \cdot V_\infty} = \frac{1 \cdot 0.0157\,\mathrm{m}}{2 \cdot 0.0356\ \frac{\mathrm{m}}{\mathrm{s}}} = 2.2\,\mathrm{s} \tag{5.2}$$

5.3 NACA0015 airfoil

5.3.1 Grid

The grid generation for the NACA 0015 airfoil was similar to the previous validation case, except this time a C-grid was used in the near-body region. Due to the sharp trailing edge an O-grid would not have sufficient resolution in the airfoil wake.

The C-grid consists of 25900 cells and extends to approximately 10 m around the airfoil. The unstructured grid consists of 43170 cells and extends from the edge of the C-grid out to the outer boundaries at $y = \pm 20\,\mathrm{m}$ and $(-25\,\mathrm{m} < x < 35\,\mathrm{m})$, giving a total of 69070 cells. On the surface of the airfoil the cells have a length of 0.0089 m and a height of 0.01 m.

The airfoil, with chord length $c = 1\,\mathrm{m}$, was positioned at a zero angle-of-attack compared to the boundaries, while the air was sent in at an 20° angle compared to the boundaries. The C-grid is aligned with the airflow, ensuring maximum spatial resolution in the wake. Figure 5.3 shows the grid, as well as a zoomed-in view of the area close to the airfoil.

A problem area on this grid is the region where the centre-line of the C-grid behind the cylinder meets the unstructured grid. Here highly skewed cells are generated. Another problem area is found where the lines extending perpendicularly from the airfoil meets the unstructured grid. In this area small cells are generated, significantly increasing the amount of cells in the unstructured part of the grid, and increasing the computation time.

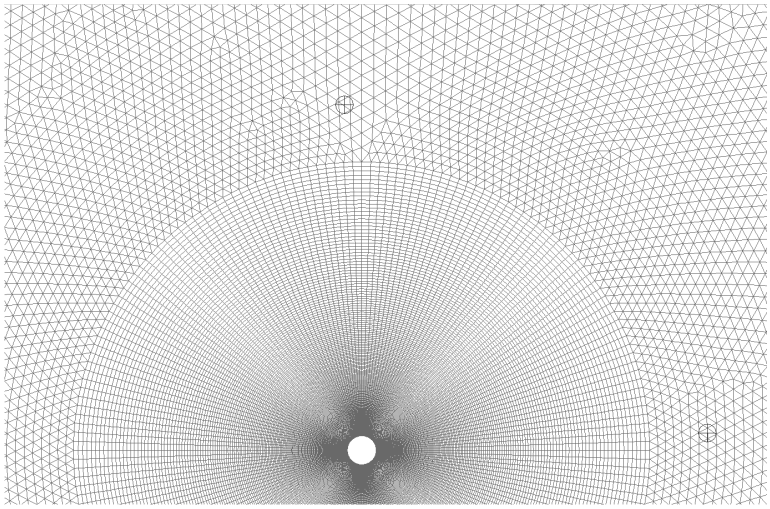

(a) overview

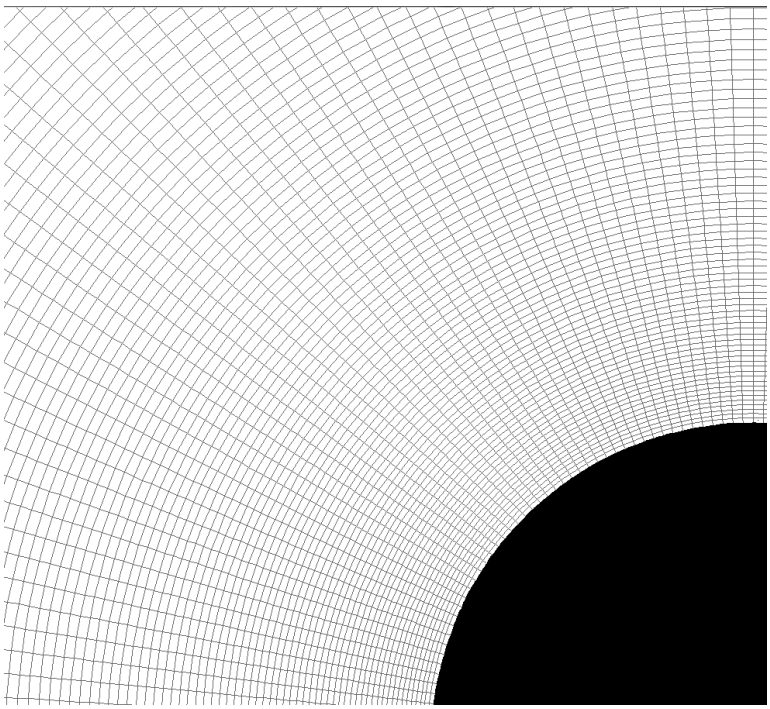

(b) detail

Figure 5.2: generated grid around the cylinder

To determine if the grid has sufficient accuracy near the airfoil the inner area of the C-grid was adapted. In the region enclosed by $x \pm 3$ and $-2 \leq y \leq 4$ all cells were split into four smaller cells. This resulted in a total of 120802 cells for the adapted grid.

5.3.2 Boundary conditions

As with the cylinder the incoming flow enters through a velocity inlet at the bottom and left boundaries and exits through a pressure outlet at the top and right boundaries, this time at $\alpha = 20°$. The inlet velocity was set to $v_\infty = 0.00534\,\frac{\mathrm{m}}{\mathrm{s}}$ to achieve $\mathrm{Re} = 300$. Using the CFL-condition (4.4) with inlet velocity, chord length and chord-wise cell size as input, Δt will be set to approximately 1.7 s.

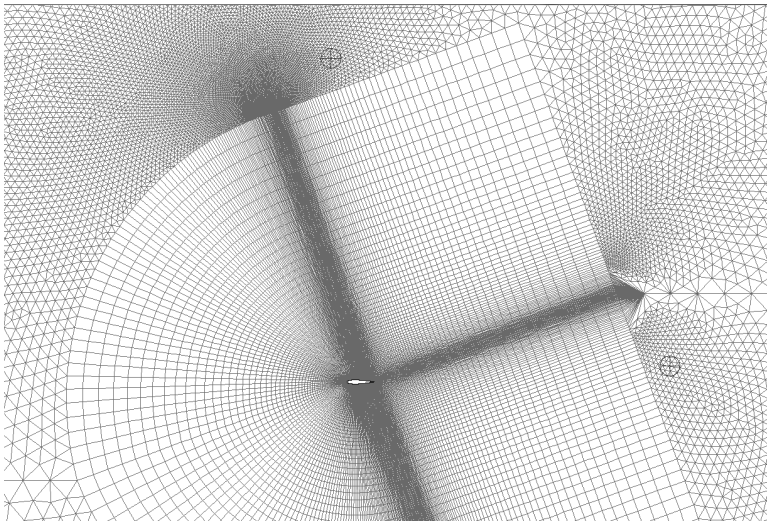

(a) overview

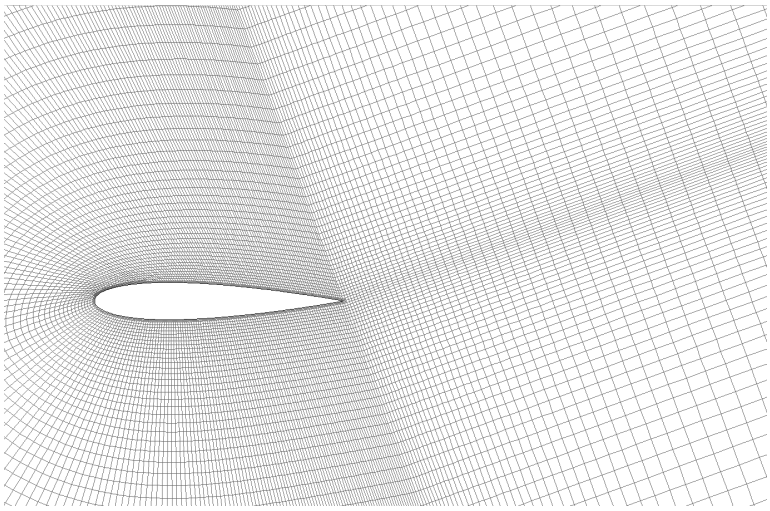

(b) detail

Figure 5.3: Grid around the NACA0015 airfoil

Chapter 6

Results and discussion

6.1 Cylinder

6.1.1 Flow

Before comparing the results of the simulations to the reference values the lift coefficient, C_l, was computed on the original and adapted grid to determine if the chosen grid had sufficient resolution to ensure a grid-independent solution.

The relative difference in amplitude and period of c_l between the original mesh (OM) and the adapted mesh (AM) is

$$\text{(amplitude)} \qquad \frac{A_{OM} - A_{AM}}{A_{OM}} = \left| \frac{(2.0054 - 1.9947) \cdot 10^{-5}}{2.0054 \cdot 10^{-5}} \right| = 0.0053 \approx 0.5\%$$

$$\text{(period)} \qquad \frac{p_{OM} - p_{AM}}{p_{OM}} = \left| \frac{1380\,\text{s} - 1401\,\text{s}}{1380\,\text{s}} \right| = 0.0152 \approx 1.5\%$$

These differences are considered small enough to use the original grid. The extra computational effort in using the adapted mesh is not worth the small gain in accuracy. All further calculations are performed on the original mesh, including the computations at Re = 150.

Several characteristic values, such as Strouhal number (nondimensional shedding frequency), magnitude of c_l and c_d and acoustic magnitude at multiple receiver positions, were examined to validate the results for the two-dimensional cylinder flow. They were compared to results by Müller [14] and Shen, Michelsen and Sørensen [12].

To determine the shedding frequency C_l was plotted against time, Figure 6.1, and the period was extracted. For Re = 150 C_l has a period of 2084s, and for Re = 200 C_l has a period of 1380s. The shedding frequency is then be the inverse of the period, or $4.798 \cdot 10^{-4} \frac{1}{\text{s}}$ for Re = 150 and $7.246 \cdot 10^{-4} \frac{1}{\text{s}}$ for Re = 200.

The frequencies were non-dimensionalised using the Strouhal number $\left(\mathrm{St} = \frac{fd}{U}\right)$

$$(\mathrm{Re} = 150) \qquad \mathrm{St} = \frac{4.798 \cdot 10^{-4}\,\frac{1}{\mathrm{s}} \cdot 1\mathrm{m}}{0.00255\,\frac{\mathrm{m}}{\mathrm{s}}} = 0.188$$

$$(\mathrm{Re} = 200) \qquad \mathrm{St} = \frac{7.246 \cdot 10^{-4}\,\frac{1}{\mathrm{s}} \cdot 1\mathrm{m}}{0.00356\,\frac{\mathrm{m}}{\mathrm{s}}} = 0.204$$

Strouhal numbers should usually lie close to 0.20 for $10^2 < \mathrm{Re} < 10^7$, with the value at Re = 200 being slightly higher than the value at Re = 150 [15]. This effect is clearly seen in the simulation results, indicating the the predicted shedding frequency is correct. The reference value of St for Re = 150 and M = 0.1 is 0.1836 while that at M = 0.2 is 0.1831. Since the flow computation is incompressible the first value will be used for comparison, giving a relative error of 2.4 %. For Re = 200 the reference value is St = 0.195, resulting in a relative error of 4.6 %.

The values of C_l and C_d are also of interest, see Figure 6.1 for a plot of C_l and C_d. Note that a slight anomaly is seen in C_l, with its mean at $\overline{C_l} = 0.06$ instead of the expected 0. In the analysis below the mean value has been subtracted from the instantaneous value to obtain a result centred around zero. The modified C_l is then compared to the literature.

$$\mathrm{Re} = 150 \qquad \max(C_l) = 0.577$$
$$\mathrm{mean}\,(C_d) = \overline{C_d} = 1.320$$

$$\mathrm{Re} = 200 \qquad \max(C_l) = 0.791$$
$$\overline{C_d} = 1.359$$

The reference value of $\overline{C_d}$ at Re = 150 is approximately 1.32 at M = 0.1 and 1.34 at M = 0.2 [14]. The obtained result is close to the low Mach-number prediction, which is to be expected as the simulations were performed using incompressible equations. For Re = 200 the reference value of the $\overline{C_d}$ is 1.33, while the computed result is 1.364 a relative error of 2.5 %.

The result for $\max(C_l)$ is reasonably close, with the simulations giving a value of 0.577 and the predicted value being 0.52. This gives a relative error of approximately 11 %.

In total the errors for the flow solutions for the circular cylinder at Re = 150 and Re = 200 are within acceptable limits, with the amplitude of the lift coefficient standing out as having the largest relative error.

6.1.2 Acoustics

For the acoustic solution receivers were placed 12 meters downstream and 12 meters cross-stream of the cylinder, resulting in receivers at $(x, y) = (11.985, 0.599)$ and $(x, y) = (-0.599, 11.985)$. The results were then nondimensionalised using the

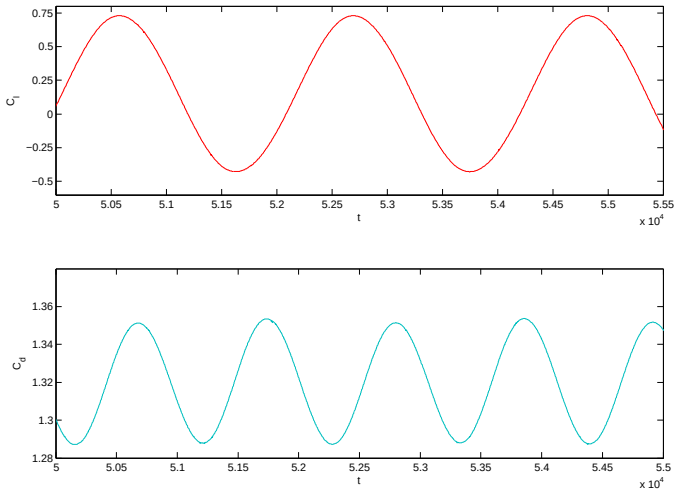

Figure 6.1: History of C_l and C_d for cylinder at Re = 150

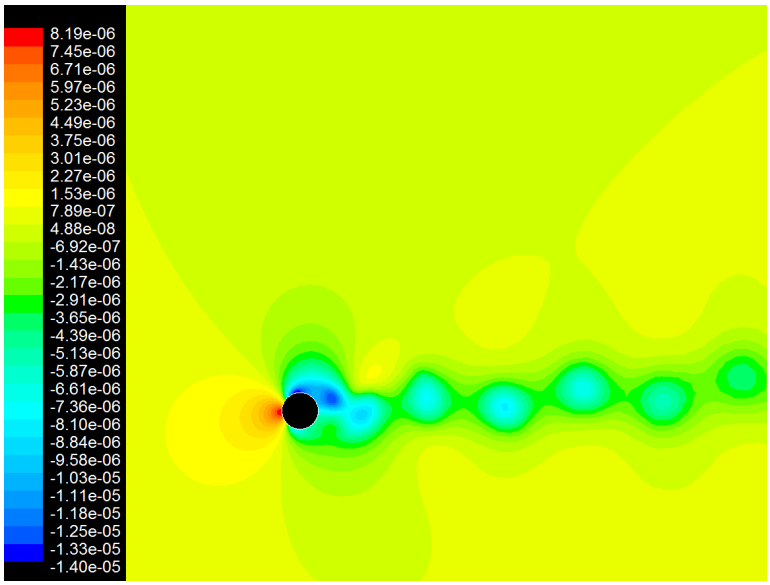

Figure 6.2: Contours of static pressure [Pa] around the cylinder at Re = 200

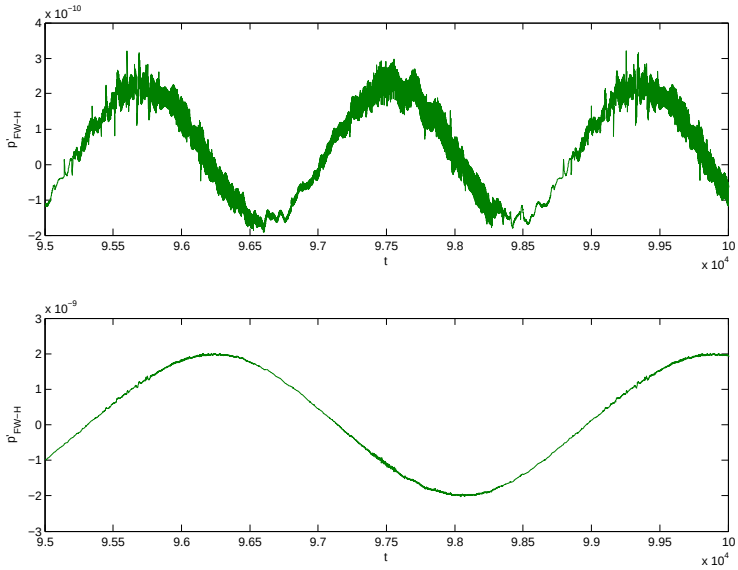

Figure 6.3: Nondimensional pressure fluctuation $(\frac{p-\overline{p}}{\rho_\infty c_\infty^2})$ for the cylinder at Re = 150, M = 0.2 in the points $(x, y) = (11.985, 0.599)$ (top) and $(x, y) = (-0.599, 11.985)$ (bottom)

density, ρ and the speed of sound, c_∞, and normalized using the mean pressure $\overline{p} = \frac{1}{N_p}\sum_{i=1}^{N_p} p'(x, y, N_i)$, where N_p is the amount of time steps in one period.

The main acoustic frequency cross stream is equal to the the frequency of C_l, while downstream the main frequency is equal to that of C_d. This is not surprising, as the downstream receiver will be affected by two vortices with opposite rotation for every major perturbation of the system. Both pressure graphs contain a high frequency signal on top of the main signal. By examining the Fourier transform of the audio signal, Figure 6.4, we find that this signal is a broadband signal, with a peak just below $f = 0.3\,\text{Hz}$.

This peak might be due to some physical phenomenon, but it might also caused by numerical errors as the time step was at $\Delta t = 0.35\,\text{s}$ for the flow computation. Since the magnitude of the pressure fluctuations is very small, they could also be the result of operating in the vicinity of machine accuracy at 10^{-16}. The amplitude of the high-frequency signal is in the order of 10^3 Pa, or 10 dB, weaker than the main fluctuation. Note that the amplitude in Figure 6.4 is not dimensionless and cannot be directly compared to that of Figure 6.3.

A comparison with the results from Müller [14] shows that the amplitude of the predicted pressure is close to the reference pressure. For Re = 150 the predicted pressure nondimensional pressure fluctuation at $(x, y) = (11.985, 0.599)$ is in the

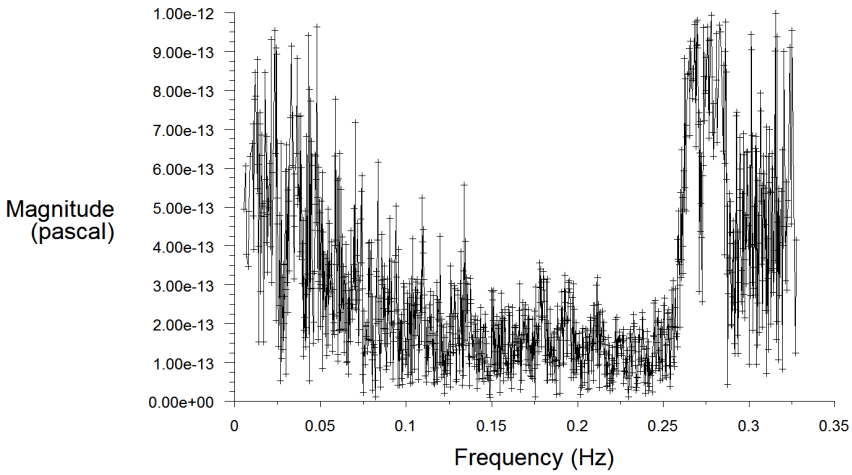

Figure 6.4: Fourier transform of the signal at $(x, y) = (11.985, 0.599)$ shown in Figure 6.3

order of 10^{-3}, and the result obtained from the flow solution is $1 \cdot 10^{-3}$. At $(x, y) = (-0.599, 11.985)$ the reference pressure is in the order of 10^{-4} and the result from the simulation is $8 \cdot 10^{-5}$.

At both of these points the pressure as given by the flow solution is larger than the pressure predicted by FW-H, and no further insight is gained into the accuracy of the FW-H-solution. Even so, the results are close to the reference.

For $\mathrm{Re} = 200$ the result is in the order of 10^{-4} for both receiver locations. The computed values fit well at $(x, y) = (-0.599, 11.985)$ with a value of $1.6 \cdot 10^{-4}$, but at $(x, y) = (11.985, 0.599)$ the result is in the order of 10^{-3}.

6.2 Airfoil

6.2.1 Flow

A comparison between the results for the original mesh and the adapted mesh indicates that the original mesh is sufficient. There is a relative difference in the average value of C_l of 1.2 %, and a difference in the amplitude of C_l of 0.4 %. From this the original mesh is considered sufficient.

A comparison with the reference value however show a large error of C_l. The predicted value is 0.3756 while the computed value is 0.6234, giving a relative error of 70.5 %. The size of the error might partly be explained by the difficulty of correctly predicting the separation bubble on the airfoil, but this claim is only speculation and not verified further.

The calculated Strouhal number is 0.591 while the reference Strouhal number is 0.435, resulting in a relative error of 36 %. The shedding frequency will determine

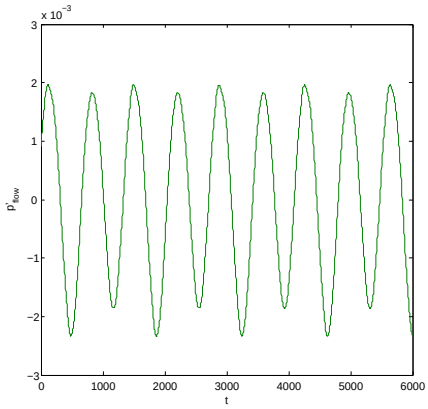

(a) Nondimensional pressure calculated from flow at $(x, y) = (11.985, 0.599)$

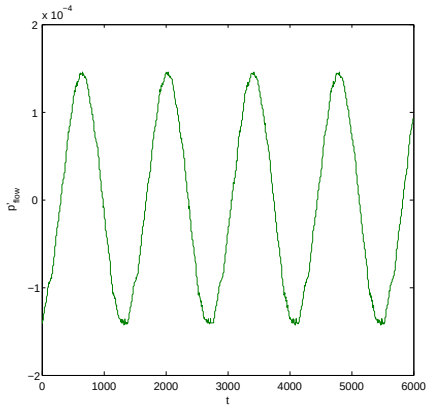

(b) Nondimensional pressure calculated from flow at $(x, y) = (-0.599, 11.985)$

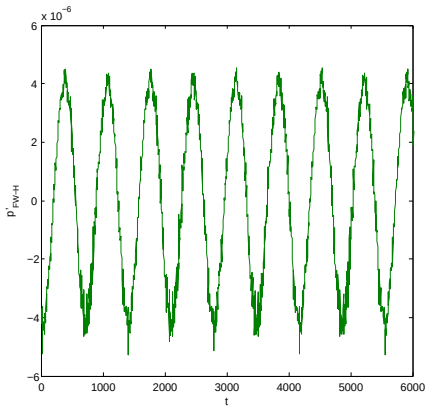

(c) Nondimensional pressure calculated by FW-H at $(x, y) = (11.985, 0.599)$

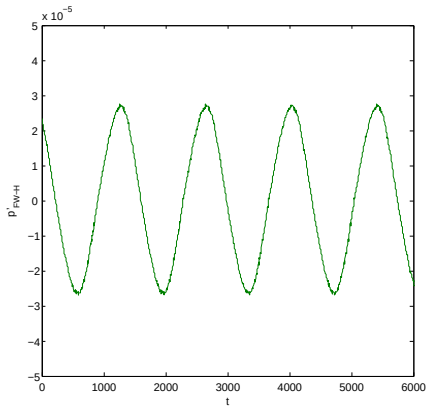

(d) Nondimensional pressure calculated by FW-H at $(x, y) = (-0.599, 11.985)$

Figure 6.5: Nondimensional pressure $\left(\frac{p-\overline{p}}{\rho_\infty c_\infty^2}\right)$ for circular cylinder at Re = 200 and M = 0.2

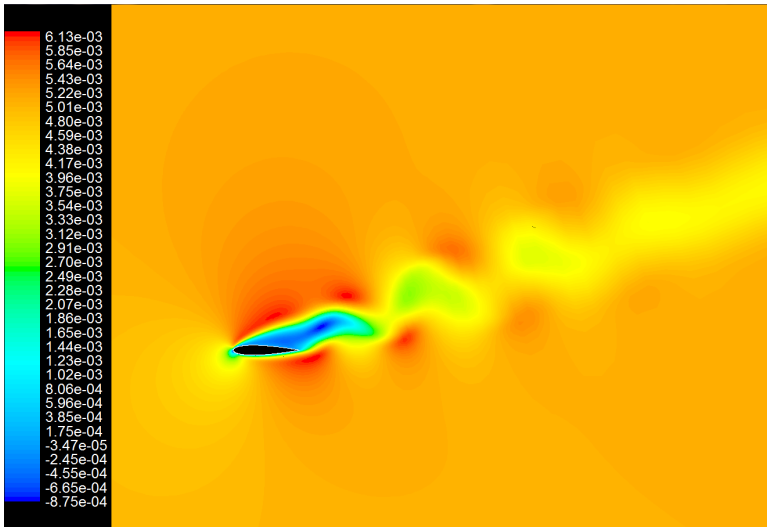

Figure 6.6: Contour of x-velocity v_x $\left[\frac{\mathrm{m}}{\mathrm{s}}\right]$ around NACA 0015 airfoil at $\mathrm{Re} = 300$

the frequency of the main acoustic signal, so the large error in fluctuation frequency will carry over to the acoustic frequency.

6.2.2 Acoustics

To compute the acoustic solution receivers were placed 12 chord lengths away from the airfoil, at $(x, y) = (11.35, 3.89)$ and $(x, y) = (-3.89, 11.35)$. This corresponds to a point along the flow direction and a point perpendicular to the flow direction.

In Figure 6.8 the pressures at these points are plotted against time. p'_{flow} is computed from the flow solution itself, while $p'_{\text{FW-H}}$ is computed using the Ffowcs-Williams Hawkings solver in FLUENT.

At the downstream position the majority of the pressure fluctuation is caused by the vortices in the flow itself, with the amplitude of p'_{flow} being in the order of 10^1 larger than that of $p'_{\text{FW-H}}$. At the point perpendicular to the the flow however the two contributions are of a similar order of magnitude.

At $(x, y) = (11.35, 3.89)$ the predicted amplitude of the nondimensional pressure fluctuation is 10^{-5}, the same as that predicted by the simulations. At $(x, y) = (-0.599, 11.985)$ on the other hand the predicted nondimensional amplitude is $1 \cdot 10^{-4}$, while the amplitude of the compute pressure fluctuations is $1.1 \cdot 10^{-5}$. From this we can see that the prediction is accurate in the region dominated by flow-induced pressure fluctuations, and not so accurate perpendicular to the flow direction.

The measurement at $(x, y) = (-0.599, 11.985)$ was the first to include a significant contribution from the FW-H equation, the other measurements have included

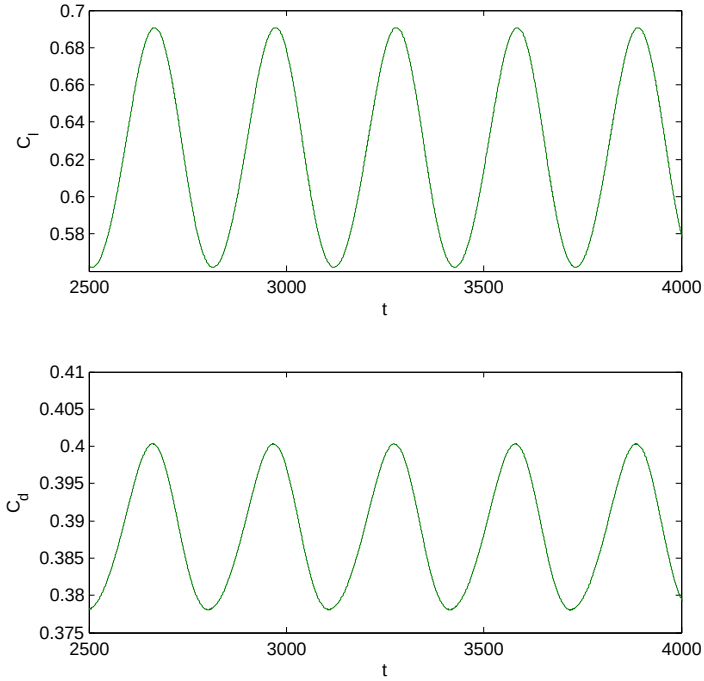

Figure 6.7: C_l (top) and C_d (bottom) for NACA 0015 airfoil at Re = 300

a large pressure fluctuation as predicted from the airflow.

The pressure fluctuation in the flow solution contain irregularities on the sinusoidal shape, as can clearly be seen in Figure 6.8a. Such irregularities are probably the result of the relatively coarse grid away from the airfoil. As expected the FW-H solution is unaffected by the grid, and does not contain such irregularities to the same degree.

The chosen test cases did not properly verify the FW-H equation in FLUENT. Further verifications need to be performed, either with receivers in other positions, or with a different flow scenario. The far-field in acoustics is defined as $r \ll L$, L is the size of the acoustic source. Here $L \approx 1\,\mathrm{m}$ and $r = 12\,\mathrm{m}$, so the receivers should already be in the far field.

As the FW-H equations are grid independent the receivers do not actually need to be situated within the computational domain and in addition the acoustic field is computed independently of the flow field. This means that the existing flow simulations can be used as the source for new acoustic computations with receivers placed at any location.

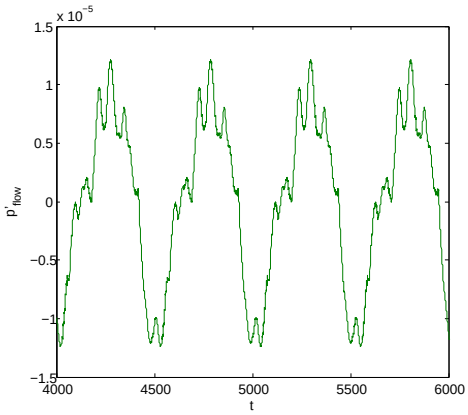

(a) Nondimensional pressure calculated from flow at $(x, y) = (11.35, 3.89)$

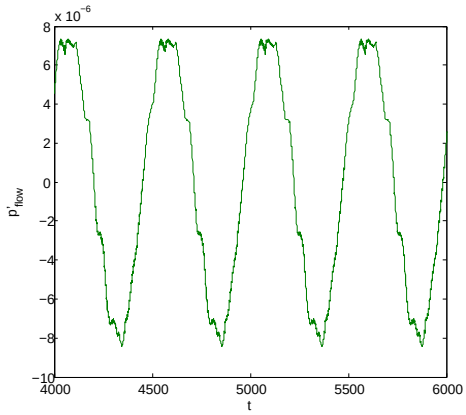

(b) Nondimensional pressure calculated from flow at $(x, y) = (-3.89, 11.35)$

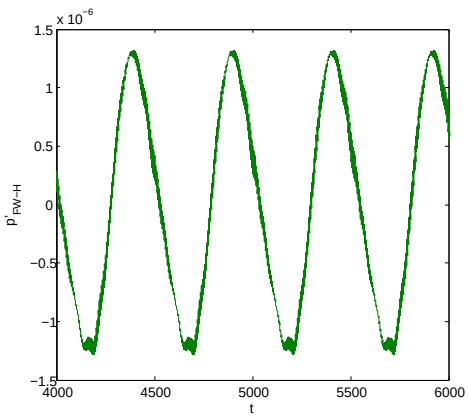

(c) Nondimensional pressure calculated by FW-H at $(x, y) = (11.35, 3.89)$

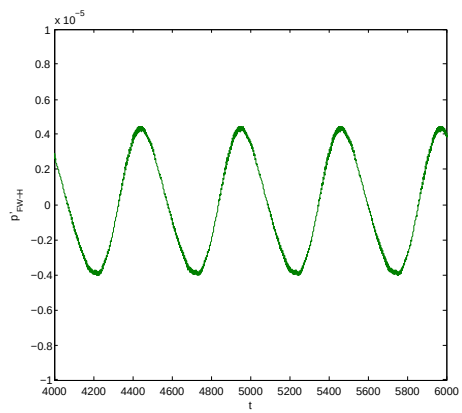

(d) Nondimensional pressure calculated by FW-H at $(x, y) = (-3.89, 11.35)$

Figure 6.8: Nondimensional pressure $\left(\frac{p-\overline{p}}{\rho_\infty c_\infty^2}\right)$ for NACA 0015 airfoil at Re = 300 and M = 0.2

Chapter 7

Conclusion

FLUENT proved to be accurate in solving the flow both in the cylinder cases and for the airfoil. The flow solution also included the required pressure information to predict the sound levels at the receiver locations.

The FW-H solver on the other was not properly verified by the chosen test cases, so no conclusion can be drawn on its efficiency in computing rotor noise from a micro UAV. Further simulations and experiments are required before such a conclusion can be drawn.

Due to the low Reynolds numbers involved for a micro UAV using DNS to compute the sound field might be feasible, although the FW-H equation or some other model is recommended to calculate the sound in the extreme far-field. The interesting far-field for the PD-100 typically stretches to around 10 m, or $\frac{10\,\mathrm{m}}{0.003\,\mathrm{m}} \approx$ 3000 chord lengths.

Further work should attempt to properly validate the FW-H solver in FLUENT for the far-field, then include unstable inlet boundary conditions and verify these, both in two- and three dimensions. Once this is done the sound generated by the tail rotor can be estimated numerically. Variations on the geometry of the tail propeller can be performed in an attempt to reduce the amplitude of the sound or to change its frequency.

As the validation cases chosen were not sufficient no predictions are made as to the sound generation of the tail propeller of the PD-100. Even so some knowledge can be gained from Chapters 2 and 3. For example we notice that BVI noise is unwanted, and can be avoided by increasing the airspeed through the propeller. Increasing the airspeed on the other hand will increase the noise from other sources.

References

[1] Y. Lian and W. Shyy, "Laminar-turbulent transition of a low reynolds number rigid or flexible airfoil," *AIAA Journal*, vol. 46, 2007.

[2] *On sound generated aerodynamnically. I. General Theory*, vol. 211, Proceedings of The Royal Society, 1952.

[3] J. E. Ffowcs Williams and D. L. Hawkings, "Sound generation by turbulence and surfaces in arbitrary motion," *Philosophical Transactions of the Royal Society*, vol. 264, pp. 321–342, 1969.

[4] L. E. Kinsler, A. R. Frey, A. B. Coppens, and J. V. Sanders, *Fundamentals of Acoustics*. James Wiley & Sons, Inc., fourth ed., 1976.

[5] H.-n. Chen, *Rotor noise in maneuvering flight*. PhD thesis, The Pennsylvania State University, 2006.

[6] K. S. Brentner and F. Farassat, "Modeling aerodynamically generated sound of helicopter rotors," *Progress in Aerospace Sciences*, vol. 39, pp. 83–120, 2003.

[7] P. Voke and M. Collins, "Forms of the generalised navier-stokes equations," *Journal of Engineering Mathematics*, vol. 18, pp. 219 – 233, 1984.

[8] A. P. Dowling and J. E. Ffowcs Williams, *Sound and Sources of Sound*. Ellis Horwood, Nov. 1983.

[9] T. Poinsot and S. M. Candel, "The influence of differencing and cfl number on implicit time-dependent non-linear calculations," *Journal of Computational Physics*, vol. 62, pp. 282 – 296, 1986.

[10] *Fluent 6.3 User's Guide*, 2006.

[11] H. Malalasekera and H. K. Versteeg, *An introduction to computational fluid dynamics - the finite volume method*. Pearson Education Limited, second ed., 2007.

[12] W. Z. Shen, J. A. Michelsen, and J. N. Sørensen, "A collocated grid finite volume method for aeroacoustic computations of low-speed flows," *Journal of Computational Physics*, vol. 196, pp. 348–366, 2004.

[13] O. Posdziech and R. Grundmann, "Numerical simulation of the flow around an infinitely long circular cylinder in the transition regime," *Theoretical and Computational Fluid Dynamics*, vol. 15, no. 2, pp. 121–141, 2001.

[14] B. Müller, "High order numerical simulation of aeolian tones," *Computers and Fluids*, vol. 34, pp. 350–362, 2008.

[15] F. M. White, *Viscous Fluid Flow.* McGraw-Hill, third ed., 2006.